

Article

Experimental and Numerical Analysis of Pile–Rock Interaction Characteristics of Steel Pipe Piles Penetrating into Coral Reef Limestone

Yongtao Zhang ^{1,2,*}, Zhiqiang Deng ^{2,3}, Peishuai Chen ^{2,3}, Huiwu Luo ^{2,3}, Ruiyuan Zhang ^{2,3}, Chengcheng Yu ^{2,3} and Caizhao Zhan ²

¹ School of Civil Engineering, Tongji University, Shanghai 200092, China

² CCCC Second Harbor Engineering Company Ltd., Wuhan 430040, China

³ Research and Development Center of Transport Industry of Intelligent Manufacturing Technologies of Transport Infrastructure, Wuhan 430040, China

* Correspondence: zhangyongtao@ccc@163.com; Tel.: +86-155-2208-3702



Citation: Zhang, Y.; Deng, Z.; Chen, P.; Luo, H.; Zhang, R.; Yu, C.; Zhan, C. Experimental and Numerical Analysis of Pile–Rock Interaction Characteristics of Steel Pipe Piles Penetrating into Coral Reef Limestone. *Sustainability* **2022**, *14*, 13761. <https://doi.org/10.3390/su142113761>

Academic Editors: Chengyu Xie, Yaguang Qin and Qingfa Chen

Received: 11 August 2022

Accepted: 19 October 2022

Published: 24 October 2022

Publisher's Note: MDPI stays neutral with regard to jurisdictional claims in published maps and institutional affiliations.



Copyright: © 2022 by the authors. Licensee MDPI, Basel, Switzerland. This article is an open access article distributed under the terms and conditions of the Creative Commons Attribution (CC BY) license (<https://creativecommons.org/licenses/by/4.0/>).

Abstract: In order to study the characteristics of pile–rock action of steel pipe driven pile in coral reef limestone stratum, coral reef limestone at the China–Maldives Friendship Bridge site was selected to carry out indoor physical and model tests with red sandstone as the control group. The test outcomes indicate the following: (1) when substantial deformation is permitted, the coral reef limestone has a considerable strength dispersion, a low post-peak stress decrease rate, and a high residual strength, roughly 30% of the peak strength; (2) when the steel pipe pile penetrates the coral reef limestone, the pile top load shows an obvious sawtooth shape, and with the increase in penetration depth, the pile end load of the high-porosity rock sample gradually decreases, and the pile end load of the low-porosity rock sample gradually increases; (3) when the steel pipe pile is penetrated, the strain value of the red sandstone is about twice that of the coral reef limestone at the same position from the steel pipe pile. These findings indicate that the high porosity and heterogeneity cementation characteristics of the coral reef limestone make the extrusion effect during piling significantly less than that of the red sandstone. In addition, the steel pipe pile penetration process is numerically simulated using a four-dimensional discrete spring model method based on the multi-body damage criterion. The numerical simulation results further demonstrate that the pile-side rock fragmentation during steel pipe pile penetration is the primary reason for the lower bearing capacity of steel pipe piles in coral reef limestone stratum. This method provides a novel approach for studying the mechanical properties of reef limestone. The findings can serve as a guide for the design and construction of steel pipe piles in the reef limestone stratum.

Keywords: coral reef limestone; steel pipe driven pile; model test; 4D-LSM; multibody failure criterion

1. Introduction

In recent years, marine engineering construction has developed fast, and coral reefs, as the only land in the distant sea, serve as the foundation of marine construction. Coral reef limestone is mainly composed of biochemical sedimentation, gravity compaction, and late cold metamorphism. In contrast to common limestone and basalt, coral reef limestone has a rough surface, high porosity, and irregular cementation [1–3]. Steel pipe driven pile construction is fast and is one of the most widely used foundation forms in the field of marine engineering [4]. However, engineering practice has shown that the load-bearing capacity of coral reef strata steel pipe driven piles is low, and in the sinking piles, the “slippery pile” phenomenon has even been observed [5–7]. Due to the unique deposition and post-evolution of coral reef limestones, the interaction law between them and steel pipe driven piles is still uncertain, which poses significant construction challenges for marine reefs. To address this issue, numerous studies have been conducted on the physical nature

and mechanical behavior of reef limestones as well as the bearing performance of steel pipe driven piles in coral reef limestone stratum.

As for the physical nature and mechanical behavior of reef limestones, the mechanical tests conducted by Zhu et al. [8,9], Liu et al. [10], and Wang et al. [11] on sandy limestones revealed that the sandy limestones with high porosity exhibited obvious compression hardening at the end of the specimens in saturated uniaxial compression tests, and the stress–strain curves even showed double peak strength and yield plateau. Uniaxial compression tests on reef limestones of various structural types from Israel showed that the strength of reef limestones was discrete, with the cracking stress ranging from 45% to 78% of the peak stress, and that the volume–strain curve was distinct from that of other types of rocks, with no obvious inflection point before reaching the peak stress, indicating a continuous body contraction before the peak [12]. Physical and mechanical tests carried out by Pappalardo [13], Palchik et al. [14], and Elhakim [15], based on reef limestone specimens from the Sicily and Israel regions of the Mediterranean Sea, respectively, showed that porosity is an important factor affecting strength and other physical parameters, and that the unconfined uniaxial compressive strength of the rock samples exhibited high dispersion and decreased with increasing porosity.

Concerning the bearing performance of reef limestone pile foundation, through the field static load test of pile end post-grouting pile in coral reef limestone, Wan et al. [16] found that the post-grouting technique can be applied to the coral reef limestone stratum, which can effectively improve the bearing capacity of pile foundation and decrease the settlement. Li et al. [17] and Liu et al. [18], through the direct shear test of coral reef limestone concrete with three interface contact states, found that the shear phenomena at the smooth and mud-filled interfaces between the coral reef limestone and concrete were characterized by the interface slip failure mode. The mud at the interface acted as a lubricant and greatly reduced the shear strength. Ghazali [19] conducted a comparative test of post-boring and post-grouting piles and driven piles on coral reef limestone strata near the Red Sea and reported that the bearing capacity of post-boring and post-grouting piles were significantly greater than that of driven piles. Using a reef limestone friction pile model test, Liu et al. [20] obtained the variation law of the bearing capacity of the model pile with the displacement of pile end. Under low circumferential pressure, the residual lateral friction resistance of reef limestone is positively correlated with the saturated uniaxial compressive strength. As the circumferential pressure increases, the residual lateral friction resistance is more affected by the circumferential pressure.

Currently, the majority of pile driving investigations on coral reef limestone strata rely on field tests, which are costly, and the penetration process is not easy to observe. The four-dimensional discrete spring model based on the multi-body damage criterion is used to simulate the penetration process, and the damage mode is utilized to reveal the reasons for the low bearing capacity of the steel pipe pile in the coral reef limestone, which serves as a foundation for the subsequent construction of marine reefs.

2. Coral Reef Limestone Physical and Mechanical Property Tests

The coral reef limestone in this study was taken from the site of the China–Malaysia Friendship Bridge located in Male, the capital of Maldives. Red sandstone was obtained from the Ezhou area in Hubei Province, China.

2.1. Specific Gravity and Density Test

Coral reef limestone cores of adjacent depths were selected, processed into standard cylindrical specimens with a diameter of 50 mm and a height of 100 mm, and numbered. The coral reef limestone specimens were numbered JB-1–JB-10, and for comparison tests, granular clastic red sandstone with typical terrestrial source pore type cementation was selected.

The specific gravity test was conducted according to the Chinese specification of rock test [21] (MWR-PRC, 1999), using the specific gravity bottle method. Coral reef limestone

and red sandstone specimens were ground into powder samples with particle sizes less than 0.075 mm, and kerosene was used as the test solution. The test results indicated that the average specific gravity of coral reef limestone was 2.65, and the average specific gravity of red sandstone was 2.66.

The density test was conducted in accordance with the Chinese specification of rock test [22] (MWR-PRC, 2020) with the volumetric method, using vernier calipers (accuracy 0.02 mm) to accurately measure the size of the standard specimen and compute its volume. The specimens were dried in an oven at 105 °C until the mass remained constant, and the dry density and porosity of the specimens were measured by weighing the mass of the specimens using a balance with an accuracy of 0.01 g on a scale.

After the test, the specimen was placed in a room to absorb moisture and stabilize before being placed in a vacuum saturation tank for vacuum saturation. The specimen was saturated at a negative pressure of 100 kPa for 4 h and then left for 4 h after removal, and weighed after wiping off the surface moisture, accurate to 0.01 g. The saturated water absorption and saturation density of the specimen were calculated.

Table 1 contains the test results. The development of internal pores is a remarkable feature of coral reef limestones [23,24]. Porosity is one of the most significant physical indicators of coral reef limestones, as illustrated in Figure 1. As porosity increases, the dry density of coral reef limestone specimens reduces in a linearly negative correlation, whereas saturation water absorption increases in a linearly positive correlation. The material heterogeneity induced by the unique deposition of coral reef limestone is far greater than that of red sandstone. As indicated in Table 2, the average porosity of coral reef limestone is much greater than that of red sandstone (11.1%), and the overall standard deviation of coral reef limestone porosity is 5.219, which is also much larger than that of red sandstone.

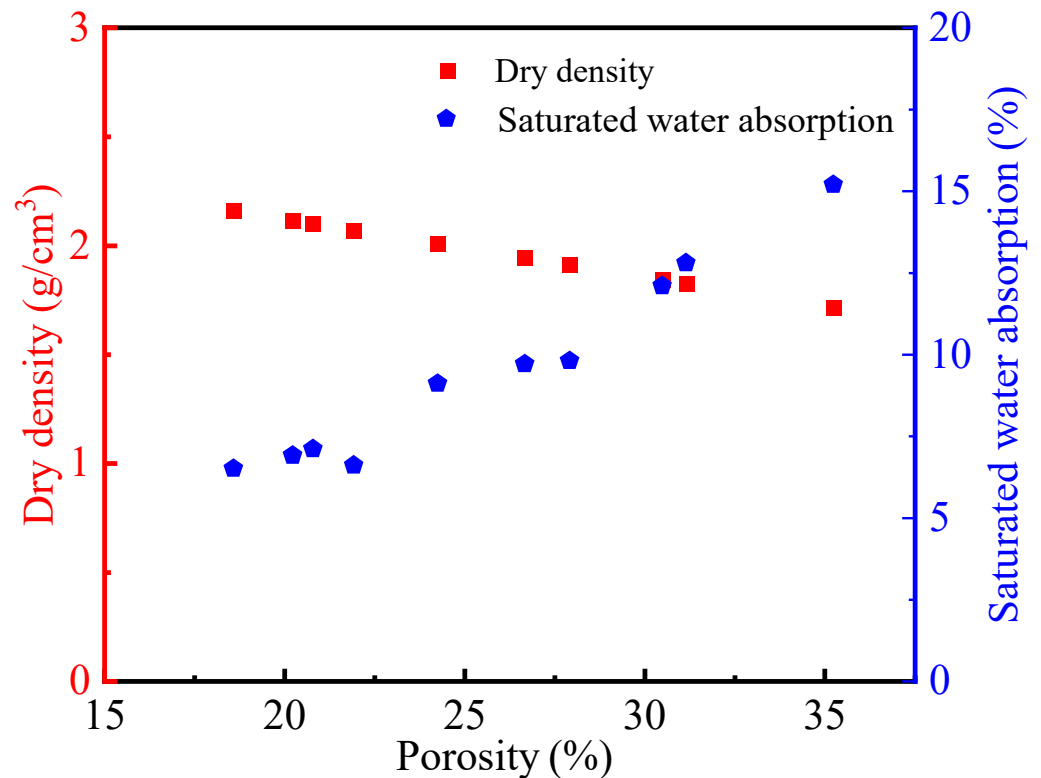


Figure 1. Porosity of coral reef limestones versus dry density and saturated water absorption.

Table 1. Physical test results of coral reef limestone and red sandstone samples.

Rock Category	Rock Sample Number	G_s	ρ_d /($g \cdot cm^3$)	ρ_{sat} /($g \cdot cm^3$)	ω_{sa} /%	n /%
Coral reef limestone	JB-1	2.65	1.94	2.13	9.7	26.7
	JB-2		2.16	2.29	6.5	18.6
	JB-3		2.11	2.26	6.9	20.2
	JB-4		1.84	2.06	12.1	30.5
	JB-5		2.01	2.19	9.1	24.3
	JB-6		2.07	2.2	6.6	21.9
	JB-7		1.91	2.09	9.8	27.9
	JB-8		1.82	2.05	12.8	31.2
	JB-9		1.72	1.97	15.2	35.3
	JB-10		2.10	2.25	7.1	20.8
Red sandstone	HB-1	2.66	2.34	2.45	4.5	11.9
	HB-2		2.39	2.49	4.1	10.0
	HB-3		2.36	2.45	4.2	11.4

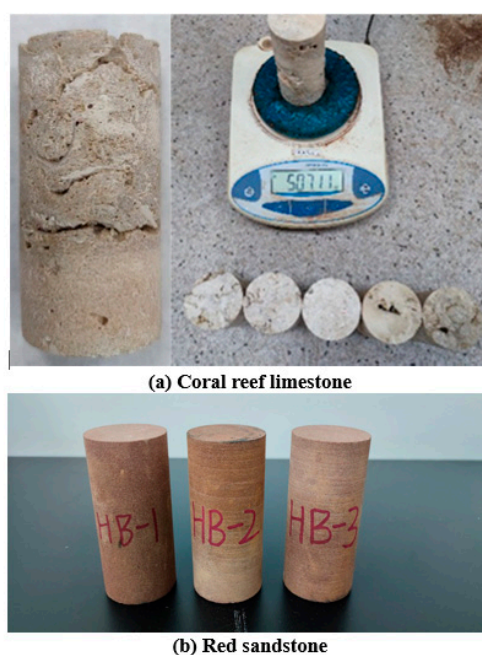
Note: G_s is the specific gravity; ρ_d is the dry density; ρ_{sat} is the saturation density; ω_{sa} is the saturation water absorption; n is the porosity.

Table 2. Characteristic statistics of coral reef limestone and red sandstone samples.

Rock Type		n /%	UCS/MPa	E/GPa
Coral reef limestone	Average value	25.73	15.15	12.73
	Overall standard deviation	5.21	6.18	5.22
Red sandstone	Average value	11.10	31.77	7.50
	Overall standard deviation	0.804	1.11	0.29

2.2. Saturated Uniaxial Compressive Strength Test

As a main characteristic parameter of rock mechanics, the uniaxial compressive strength of rocks has been widely utilized in engineering practice. Utilizing TSZ-6A fully automatic strain-controlled triaxial equipment, the unconfined saturated uniaxial compressive strength test was conducted. As shown in Figure 2, the specimen had a diameter of 50 mm and a height of 100 mm. It was loaded using a displacement-controlled method with a loading rate of 0.002 mm/s, and 13 sets of tests were completed. Under axial compression load, mechanical parameters such as saturated uniaxial compressive strength UCS, modulus of elasticity E , and peak strain ϵ_p of the coral reef limestone and red sandstone specimens were determined. The stress–strain curves of the specimens are depicted in Figure 3, and the statistical results of the tests are presented in Table 3.

**Figure 2.** Rock specimen.

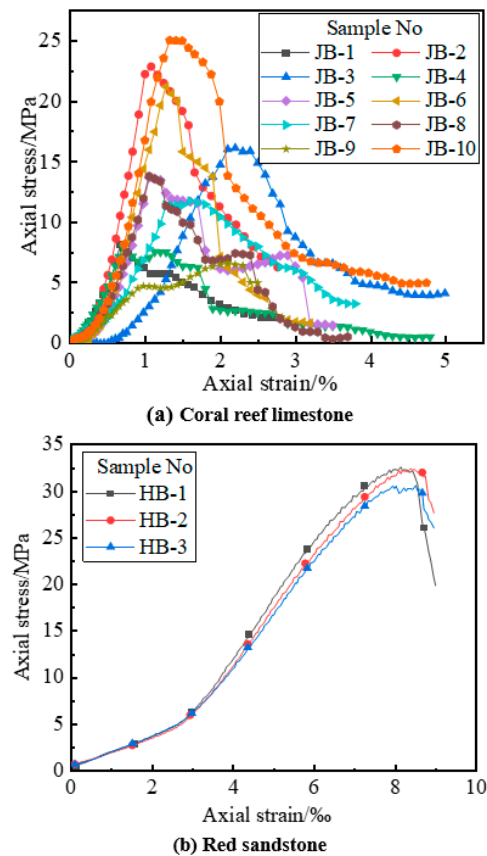


Figure 3. Saturated uniaxial compressive stress–strain curves for red sandstone and coral reef limestone.

Table 3. Saturated uniaxial compression test results.

Rock Category	Rock Sample Number	UCS/MPa	ε_p /%	E/GPa
Coral reef limestone	JB-1	8.2	0.66	12.3
	JB-2	23.6	1.07	21.2
	JB-3	16.1	2.19	7.8
	JB-4	8.3	0.70	11.1
	JB-5	14.2	1.05	13.2
	JB-6	21.6	1.27	17.7
	JB-7	12.5	1.59	7.9
	JB-8	14.9	1.05	13.3
	JB-9	7.0	2.09	3.6
	JB-10	25.1	1.32	19.2
Red sandstone	HB-1	32.6	8.1	7.9
	HB-2	32.5	8.2	7.4
	HB-3	30.2	7.8	7.2

Note: UCS is the saturated uniaxial compressive strength; ε_p is the peak strain; E is the modulus of elasticity.

Ten sets of coral reef limestone samples and three groups of red sandstone samples were subjected to saturated uniaxial compression testing. As depicted in Figure 3a, the axial stress–strain curve of coral reef limestone specimens exhibited a linear growth trend before reaching the ultimate strength, and after reaching the peak strength, the specimens did not sustain complete damage, and their bearing capacity gradually decreased and strain further increased, with a low post-peak stress drop rate. Coral reef limestone has large residual strength. As shown in Figure 3b, the peak strength of the red sandstone specimen is relatively stable at approximately 31 MPa, and the damage form is typical of brittle damage. The axial stress–strain curve exhibits a linear growth trend in the early

stage of loading, and the strength decreases quickly after reaching the peak strength, with no residual strength.

As indicated in Table 2, the strength and elastic modulus of the coral reef limestones are low and widely distributed, with peak strength ranging from 7.0 MPa to 25.1 MPa and elastic modulus ranging from 3.6 GPa to 21.2 GPa, with strong dispersion. The coral reef limestones have a substantially larger standard deviation of the UCS and elastic modulus than that of the red sandstone. This is due to the unique diagenesis and post-evolution of the coral reef limestone, whose strength is mainly determined by the strength of the constituent minerals, the degree of cementation, and the development of primary fractures. Due to the different porosity, the specimens are saturated with water, and the water between the pores contains distinct water. Under axial stress, the water between the pores weakens the frictional strength between the cemented particles and accelerates the development of the rupture surface, resulting in coral reef limestone damage under a small axial stress. As shown in Figure 4, with the increase in porosity, the strength of coral reef limestone decreases with an exponential negative correlation, which is close to the experimental results of Liu et al. [18]. The saturated water absorption of samples with a high porosity is generally higher, whereas the peak stress strength is lower. In addition, the unique pore structure of the coral reef limestone gives it a certain post-peak strength, and the axial strain corresponding to the peak strength is about 1.8%, which is greater than the axial strain value of 8‰ when the red sandstone reaches the peak strength.

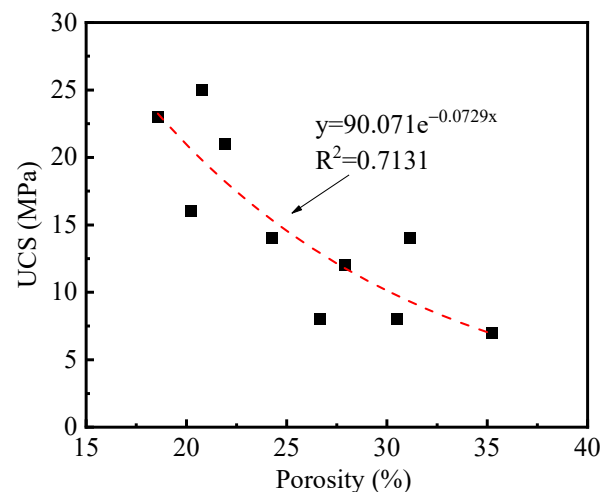


Figure 4. Relationship between saturated uniaxial compressive strength and porosity of coral reef limestone.

3. Model Test of Steel Pipe Pile Penetration into Coral Reef Limestone

In order to study the characteristics of pile–rock action during the sinking process of coral reef limestone driven pile, a seamless steel pipe was used to simulate the sinking process of the driven pile by static pressing into a coral reef limestone sample. Simultaneously, a model test of red sandstone driven pile was conducted as a comparison test.

3.1. Specimen Preparation

As depicted in Figure 5, the model pile is a DN32 seamless steel pipe pile with a 42 mm diameter and 3.2 mm wall thickness. The analogy method was used to determine the model size. Through tests, Oveson [25] found that when the inner diameter of the model box was about 5 times the foundation diameter ($b = 113.1$ mm, $D = 530$ mm, $B/b = 1.84$), the bearing capacity was 10–20% higher than expected due to the influence of the side wall. With the same model box, when $b = 79.8$ mm, the test result has no boundary effect, and $B/b = 2.82$. We quoted the boundary condition and set the ratio of the distance B (Figure 6) between the pile and the box wall to the pile size b as 3.76, which is greater than 2.82. Table 4 displays

the size and parameters of the coral reef limestone sample and red sandstone samples, with the red sandstone serving as the comparative sample.

Table 4. Parameters of coral reef limestone and red sandstone.

Rock Type	Number	Diameter/mm			Height/mm	Dry Mass/kg	$n/\%$
		on	Medium	Down			
Coral reef limestone	J-1	198.1	199.5	199.9	210	12.06	30.4
	J-2	201.2	200.9	200.2	210	13.21	25.0
Red sandstone	H-1	200.5	200.8	200.1	210	15.62	11.0

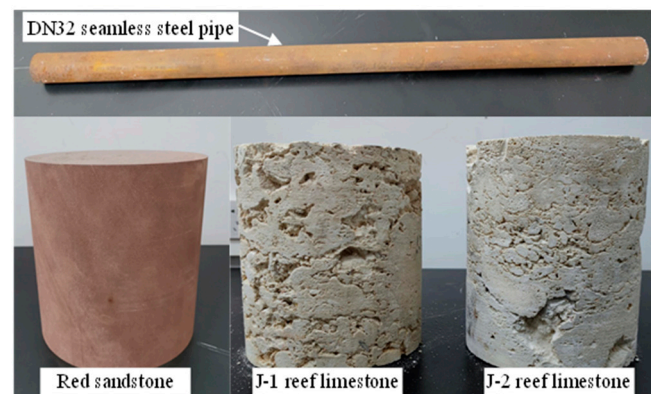


Figure 5. Model piles and rock samples.

3.2. Test Equipment and Test Methods

The model test was carried out on the WDW-1000G (floor-standing) universal testing machine produced by Shanghai Hualong Testing Instrument Co., Ltd. (Shanghai, China). The deformation was used to test the influence range of piling. The distance between the end of the rock sample and the steel pipe was controlled, and the loading rate was 0.002 mm/s.

Six BF120-60AA strain gauges were arranged symmetrically at the positions of 19 mm, 39 mm, and 59 mm of the pile, and two rows of four BF120-60AA strain gauges were placed at 60 mm and 130 mm from the top surface on the side, numbered from 1 to 10, as shown in Figure 6.

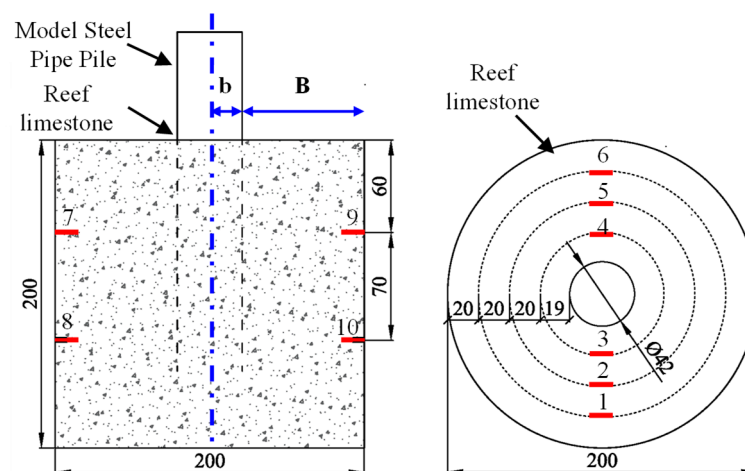


Figure 6. Strain gauge arrangement of rock samples.

In order to demonstrate the development of internal fissures in the coral reef limestone when the pile is driven into the pile and sunk, the rock specimen was filled with fissures using LS-100AB epoxy resin adhesive, and the rock specimen was then dissected along the axis after filling to demonstrate the development of internal fissures within the rock.

The test primarily determines the top load and displacement of the pile during the penetration of the driven pile, the range of effect during penetration, the rock deformation on the side of the pile, and the fracture development of the specimen. The general arrangement of the test is shown in Figure 7, which consists primarily of a rock sample, a model pile, a loading control system, and a strain acquisition system.

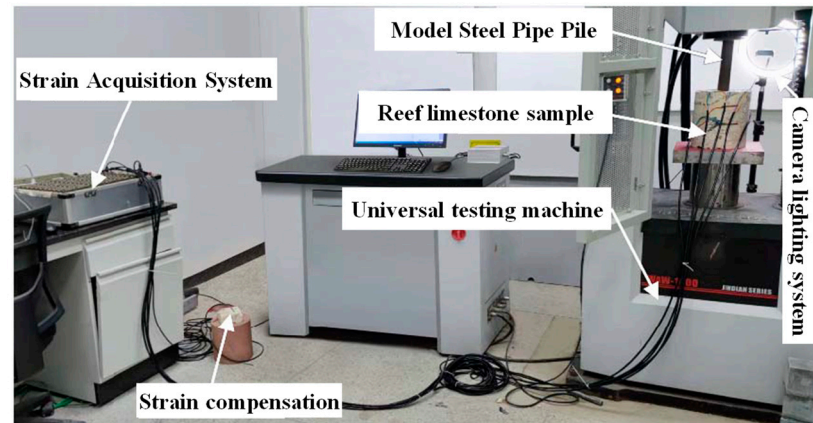


Figure 7. General layout of the test.

3.3. Test Results and Analysis

1. Pile top load and displacement during penetration

The pile top load versus displacement curve when the steel pipe pile is penetrated is shown in Figure 8. At the beginning of loading, the coral reef limestone load increases linearly. As penetration depth increases, the J-1 rock sample demonstrates obvious strain softening characteristics. The pile top load fluctuates around 15 Kn. In contrast to J-1, the J-2 rock sample demonstrates obvious strain hardening characteristics, and the pile top load fluctuates around 35 kN. The red sandstone exhibits obvious strain hardening characteristics. With penetration depth, the pile top load also increases; the increase rate is first rapid and then slow. All show obvious linear characteristics to the peak rock rupture, and then rapidly decay to 125 kN near the peak of the first stage, which is about 8.3 times that of J-1 coral reef limestone and 3.6 times that of J-2 coral reef limestone.

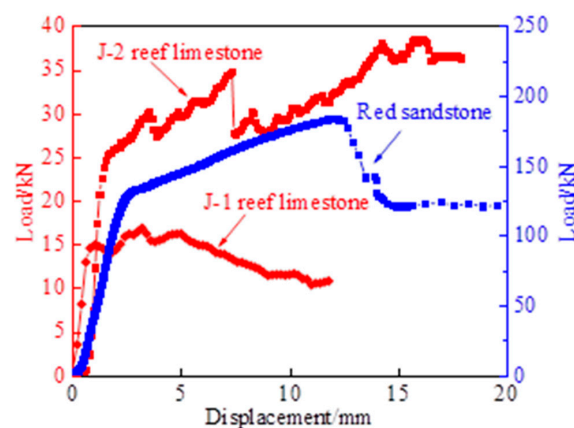


Figure 8. Relationship between displacement and load of steel pipe piles in red sandstone and coral reef limestone.

The porosity of the coral reef limestone is greater than that of the red sandstone. The steel pipe pile frequently passes through the pores throughout the penetration process, making the pile top load show a jagged change, while the pile top load changes more uniformly in the red sandstone. The porosity and disorder of distribution of J-1 are significantly larger than those of J-2; thus, the pile top load level of J-1 is significantly smaller than that of J-2, and the change trend of pile top load in rock samples of J-1 and J-2 is different, with J-1 showing a slowly decreasing trend and J-2 showing a slowly increasing trend. This is different from the increasing trend of pile top load in the lateral limit compression experiments of coral reef limestone at the pile end conducted by Liu et al. [20]. A possible reason is that the heterogeneity of coral reef limestone cementation and the formation of a weak zone by dissolution pores cause the pile top load of the J-1 coral reef limestone sample to show a decreasing trend.

2. Influence range of penetration process

During the steel pipe penetration, the peak strain occurs in the region of $0.5D$ (pile diameter), and the farther away from the center of the steel pipe pile, the smaller the strain value of red sandstone and coral reef limestone. Strain changes in different testing areas of red sandstone are illustrated in Figure 9a, where $1D$ from the pile wall is reduced to half of the peak value, and $1.5D$ from the pile wall is reduced to two-thirds of the peak value. The strain changes in different testing areas of coral reef limestone are illustrated in Figure 9b, where the strain value at $1.0D$ is reduced to three-quarters of the peak value, and $1.5D$ is reduced to one-half of the peak value. At the same position from the pile perimeter, the strain of coral reef limestone is about one-quarter to one-half that of red sandstone. This is likely because the red sandstone is a typical terrestrial sedimentary rock with a single depositional environment, the saturated uniaxial compressive strength and porosity of the rock sample vary little, and the rock is more homogeneous. The marine bio-deposition account produces the coral reef limestone, and the rock formation environment is complex. The saturated uniaxial compressive strength and porosity of the rock sample vary significantly, and coral reef limestone is relatively heterogeneous. When the steel pipe pile is penetrated, the stress is transferred with the same law and decays slowly in the relatively homogeneous red sandstone, while in the significant heterogeneity of coral reef limestone, the stress is transferred with a different law and decays more rapidly due to the high porosity and heterogeneity cementation properties. Therefore, the strain value of coral reef limestone is significantly smaller than that of red sandstone at the same position from the pile perimeter, which further indicates that the high porosity and heterogeneity cementation characteristics of coral reef limestone make the crowding effect during piling much lower than that of red sandstone.

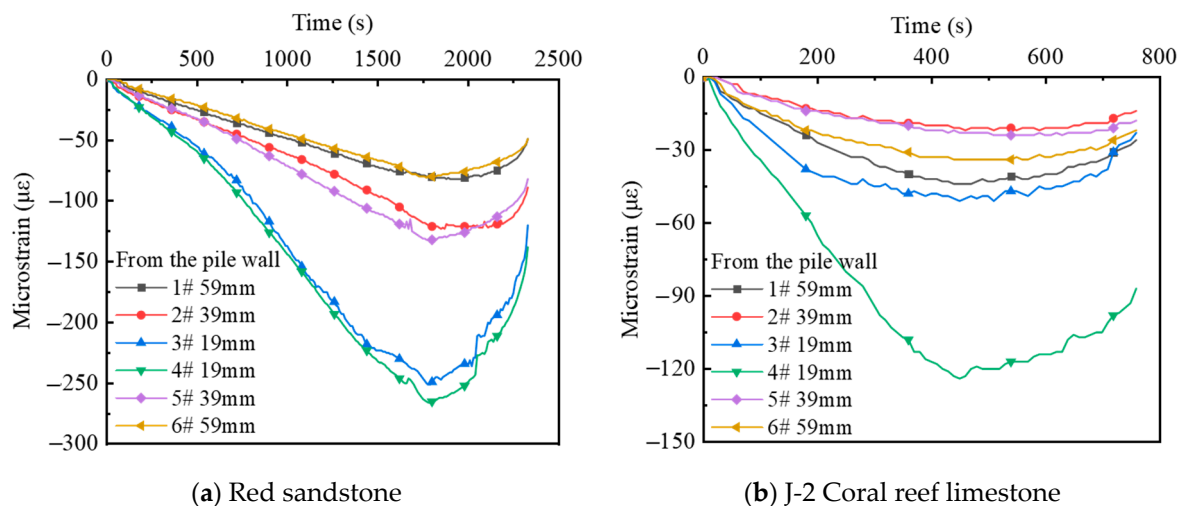


Figure 9. Red sandstone and coral reef limestone sidewall strain.

During penetration, the vertical strain gauges can be utilized to analyze the distribution pattern of stress values along the height direction. Comparing Figures 10a and 10b, it is evident that the strain values at each measurement point of the red sandstone are relatively close to each other, while the strain values on both sides of the coral reef limestone have not only positive and negative dissimilarity but also a difference of more than twofold, indicating that the stress transmission path of the coral reef limestone is more complicated than that of the red sandstone.

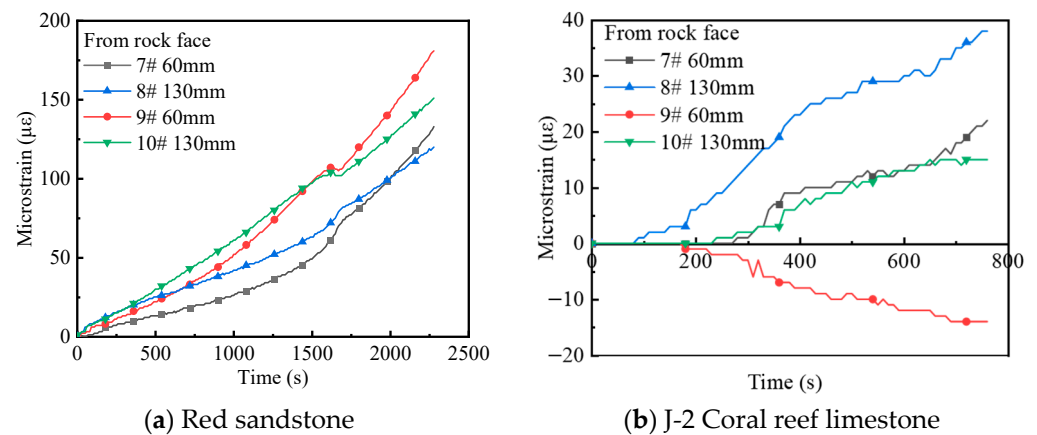


Figure 10. Strain on the upper rock face of red sandstone and coral reef limestone.

3. Coral reef limestone fracture development during pile sinking

Figure 11 depicts the damage patterns and fracture distribution of coral reef limestone and red sandstone. The surface fracture development of coral reef limestone is relatively uniform, and the rock surface is evenly divided; however, the surface fracture development of red sandstone has no obvious pattern. At the same penetration depth, the red sandstone develops penetrating fractures and the rock sample is broken as a whole; the coral reef limestone develops fractures but does not penetrate the rock sample and exhibits local damage, indicating that the red sandstone exhibits obvious brittle damage and the coral reef limestone has a weaker crowding effect than the red sandstone.

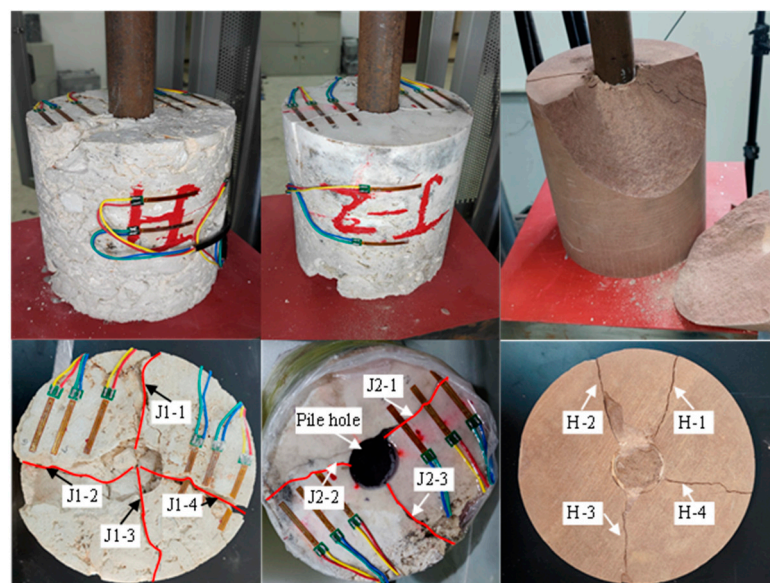


Figure 11. Rock damage form of steel pipe driven piles during pile sinking.

After removing the steel pipe at the end of the test, the pressure pile hole was filled with crystal drip glue. The crystal drip glue has sufficient fluidity and flows along the penetrating fissures inside the coral reef limestone to fill the fissures. After 24 h, the glue solidified, and the rock sample was dissected into two parts along the center of the circle with a large rock cutting machine. The damage pattern inside the rock sample is shown in Figure 12. After dissection, the internal pores of the coral reef limestone were found to be rich in shells, coral limbs, and other biological particles, indicating a clear marine bio-sedimentary accounting. Three obvious fissures developed within the J-1 coral reef limestone and connected to the fissures on the rock face; three fissures, NL1–NL3, grew within the J-2 coral reef limestone and connected to the fissures on the rock face, dividing the rock sample into four parts. The width of fracture development is positively correlated with the penetration depth of steel pipe. The penetration depth of steel pipe in J-1 coral reef limestone is about 4 cm, and in J-2 coral reef limestone, it is about 8 cm; the width of the J-1 fracture is much smaller than that of the J-2 fracture. After the model pile penetrated into the coral reef limestone, the rock on the pile side was broken, and the debris filled the model pile and the coral reef limestone hole wall. The pile wall was not close to the coral reef limestone wall, and the contact between the pile and the coral reef limestone was a point-to-point rigid contact. Therefore, the broken coral reef limestone debris provided the pile side friction resistance, and the friction resistance was low.

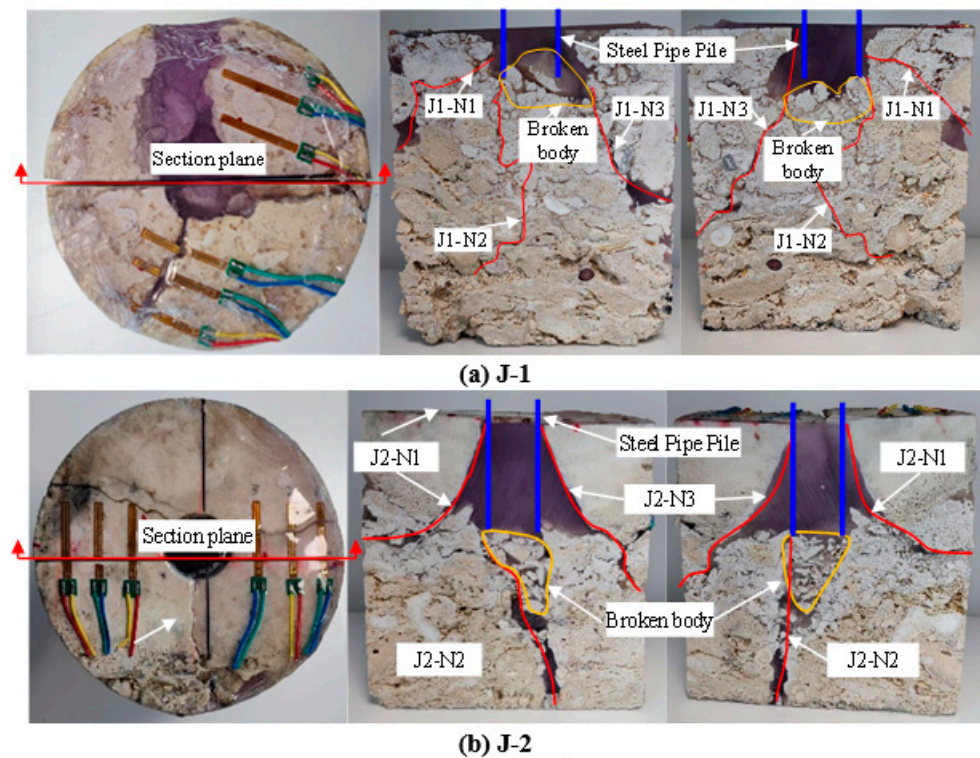


Figure 12. Internal fracture development of coral reef limestone.

4. Numerical Simulation of Steel Pipe Pile Penetration into Coral Reef Limestone

4.1. Four-Dimensional Discrete Spring Model Based on the Multi-Body Damage Criterion

By introducing four-dimensional spatial interactions, the four-dimensional discrete spring model (4D-LSM) resolves the problem of Poisson's ratio limitation in conventional LSM [26,27]. The primary distinction between 4D-LSM and classical DEM and molecular dynamics is that each particle in 4D-LSM has not only three degrees of freedom but also a fourth spatial degree of freedom, and the connection between particles must take into account the interaction in four-dimensional space. The 4D-LSM model based on the multi-

body damage criterion can be used to characterize rock-like materials in more detail by incorporating factors such as cohesion and the internal friction angle of rocks [28].

1. Multi-body damage criterion for four-dimensional spring model

In order to obtain the stress tensor equation for the spring bond, the computational model employed in 4D-LSM can be further represented as a network diagram, as shown in Figure 13. The stress state of the particle can then be characterized in a similar way to that of finding the fiber stress, i.e., the particle and its neighbors form a particle cluster, and the stress state of the particle can be represented by the deformation state of the spring bond around the particle as follows (Yin et al., 2015) [28]:

$$\sigma_{ij}^I = \frac{1}{2V^I} \sum_{j=0}^N f_i^{IJ} n_j^{IJ} l_0^{IJ} \tag{1}$$

where σ_{ij}^I is the stress tensor of particle I , V^I is the volume of particle I , f_i^{IJ} is the interaction force component between particle I and its neighboring particles, n_j^{IJ} is the normal vector component of particle I and its neighboring particles, and l_0^{IJ} is the original spring length between particle I and its neighboring particles.

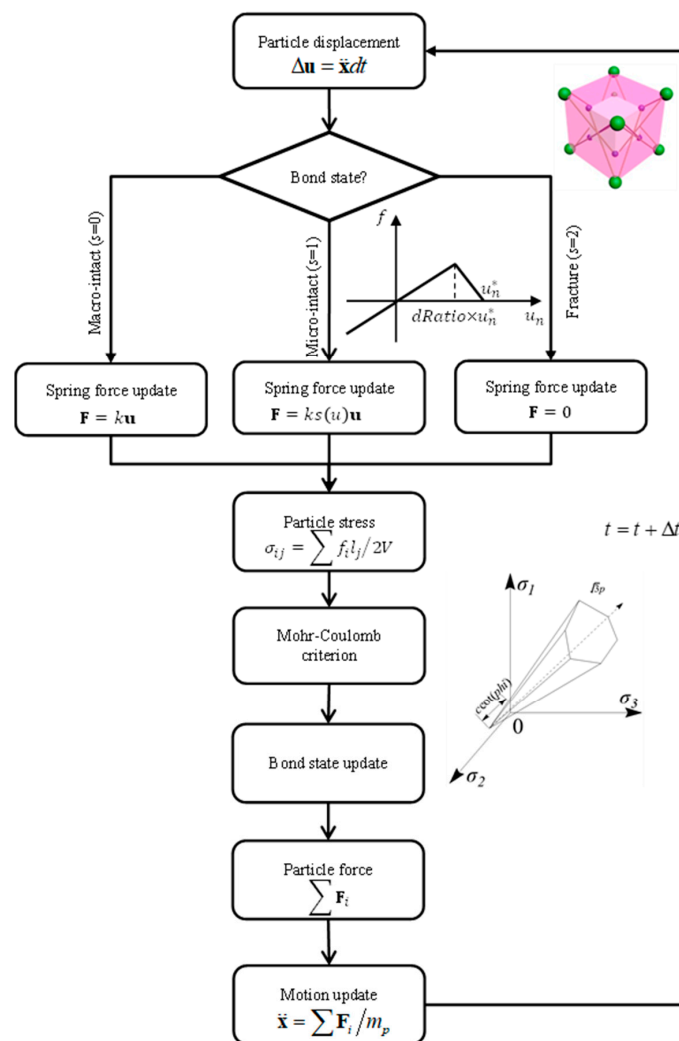


Figure 13. The 4D-LSM calculation flow based on multi-body damage criterion.

In order to determine the damage of spring bonds by introducing a macroscopic damage criterion based on stress characterization, a modified Mohr–Coulomb criterion is used in this paper.

$$f(\sigma_1^{bond}, \sigma_3^{bond}) = \begin{cases} ((1 - \sin \varphi)\sigma_3^{bond} - (1 + \sin \varphi)\sigma_1^{bond}) \\ + 2c \cos \varphi \leq 0 \\ \sigma_1^{bond} - \sigma_t^* \geq 0 \end{cases} \quad (2)$$

where $\sigma_1^{bond}, \sigma_3^{bond}$ are the first and third principal stresses corresponding to the spring bond stress tensor, φ is the internal friction angle of the material, c is the cohesion of the material, and σ_t^* is the tensile strength of the material.

2. Intrinsic model after spring bond breakage

The 4D-LSM based on the multi-body damage criterion uses a damage model to characterize the response of a spring after damage [28]:

$$f = \begin{cases} ku_n & , f(\sigma_{ij}^{bond}) < 0 \\ (1 - D)ku_n & , f(\sigma_{ij}^{bond}) \geq 0 \end{cases} \quad (3)$$

where D is the amount of damage to the spring key and is zero in the initial condition, and u_n is the elongation of the spring key.

The behavior of a spring bond once it reaches strength can be described by establishing a three-dimensional damage function for the spring bond. We define a spring intrinsic model with a linear softening phase in this study as follows [29]:

$$D(u_{3D}) = \begin{cases} \frac{u_{3D} - u_{3D}^p}{(1 - dRatio)u_{3D}}, & u_{3D} \leq u_{3D}^{max} \\ 1 & u_{3D} > u_{3D}^{max} \end{cases} \quad (4)$$

where $dRatio$ is the ratio of the spring deformation corresponding to the peak point to the final deformation, as in Figure 13, and u_{3D}^p is the deformation corresponding to the peak stress of the spring bond.

Figure 13 depicts the 4D-LSM calculation process using the multi-body failure criterion. Before calculating the strain and force on the particle, the macroscopic strength principal is used to assess whether each spring is broken. If a spring is broken, it enters the nonlinear principal calculation outlined in Equation (1); otherwise, it enters the elastic principal calculation.

4.2. Numerical Calculation Model for Macroscopic Generalization of Coral Reef Limestones

The incorporation of seawater during the deposition of coral reef limestone results in their remarkable heterogeneity. The heterogeneity of the coral reef limestone is characterized by setting different strength reduction parameters for the spring bonds of the model, which obey the Weibull distribution function commonly used to describe the fine-scale heterogeneity of defect-bearing materials such as rocks and concrete [30], as shown in Equation (5).

$$f(\zeta) = m\zeta^{m-1}e^{-\zeta^m} \quad (5)$$

where m is the material homogeneity coefficient. The value of m is related to the compressive strength, and its rule is similar to Li et al. [31]. According to the result of Figure 14b, set $m = 3$ to reduce the error of UCS strength value. ζ is a random number obeying the Weibull distribution.

A standard cylindrical model for uniaxial compression tests was established with dimensions of 50 mm in diameter, 100 mm in height, 2 mm in particle diameter, and 100,000 particles in total. As shown in Table 5, based on the test results in Section 2, a trial-and-

error method is used to select the parameters of the simulated sample. We selected the parameters closest to the test results, and the calculation results are shown in Figure 14.

Table 5. Numerical model calculation parameters.

E (GPa)	μ	Tensile Strength (MPa)	φ (°)	C (MPa)	dRatio
25	0.10	8.5	32	12.2	0.2

Note: E is the modulus of elasticity; μ is the Poisson's ratio; φ is the angle of internal friction; C is the cohesive force.

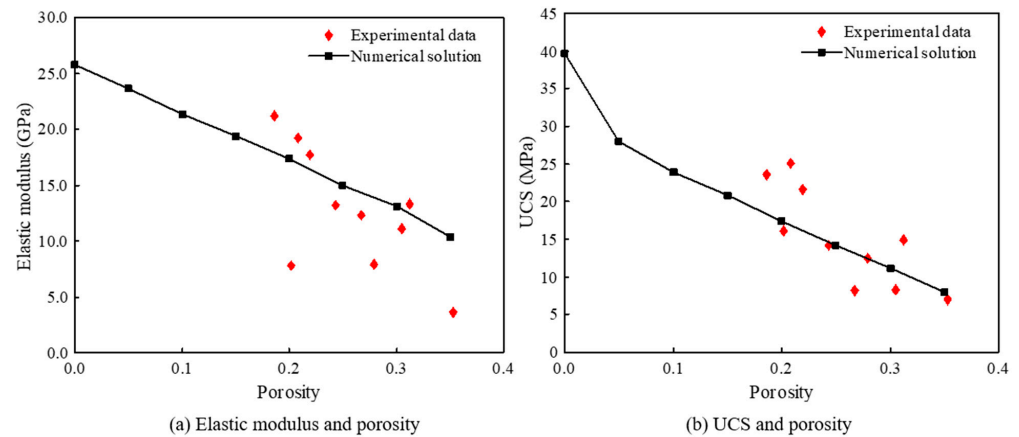


Figure 14. Comparison of numerical and experimental results.

Four standard numerical calculation models were established using the parameters in Table 5, and the porosity was 15%, 20%, 25%, and 30% in turn. The calculation results of the 25% porosity numerical model are shown in Figure 15. Two large cracks emerge in the coral reef limestone sample under load, and the damaged area (red particles) is concentrated at the end of the rock sample, which is similar to the results of the indoor test. In accordance with the stress–strain curve depicted in Figure 16, the numerically calculated uniaxial compression experiments match well with the physical tests; both exhibit linear growth before the axial stress reaches the peak, and the peak axial stress is close, but after exceeding the peak, the numerical simulation shows a deviation from the experimental ductile damage due to the dRatio in the numerical simulation affecting both strength and post-peak mechanical response [29], and excessive dRatio leads to less strength and exhibits brittle damage. In this paper, we only focus on the strength and crack extension of the material. The relationship between reef limestone characteristics and displacement can be referred to the research ideas of Xie et al. [32]

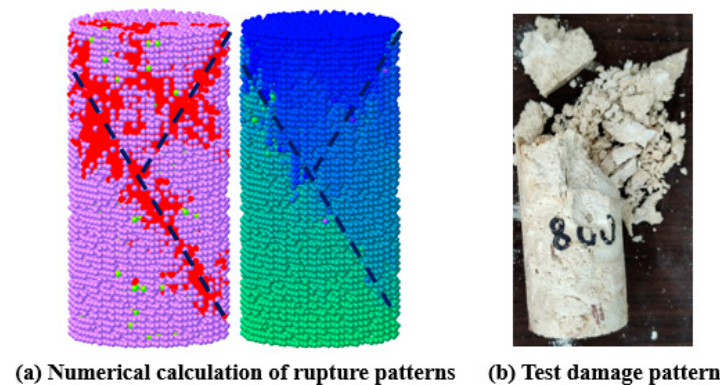


Figure 15. Comparison of numerically calculated fracture patterns of coral reef limestones with experiments.

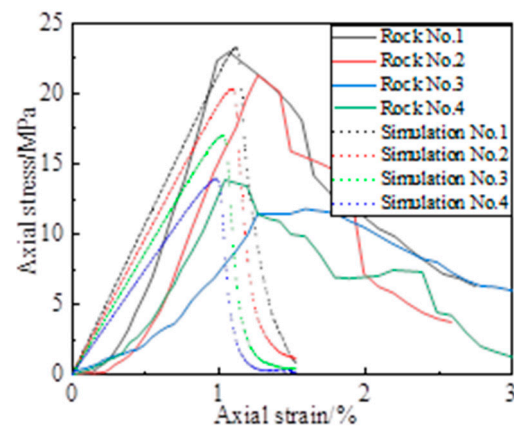


Figure 16. Comparison between numerical simulation and experimental results of uniaxial compression.

4.3. Analysis of Numerical Simulation Results

As seen in Figure 17, a numerical model of a coral reef limestone steel pipe pile penetration test was developed, with a model diameter of 200 mm, a model height of 210 mm, a particle diameter of 2 mm, and a total number of particles of around 700,000. A circular downward velocity load of 0.002 mm/s was applied at the center of the upper end face of the model with the same diameter as the steel pipe pile, and the lower boundary of the model was fixed. The material parameters are shown in Table 5.

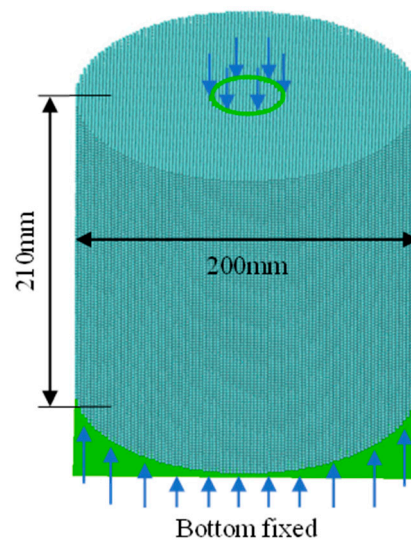


Figure 17. Numerical model of coral reef limestone steel pipe pile penetration test.

The numerical calculation results are shown in Figure 18. Under the action of vertical displacement, the coral reef limestone specimen develops four main cracks centered on the loading circle (Figure 18c), which divide the rock end face into four areas and gradually connect. As the loading continues, the fifth secondary crack begins to develop (Figure 18a), and the rock specimen is finally destroyed. The angle and direction of the crack development are close to the physical test results. The particles near the loading circle area were damaged and formed a ring-shaped fracture zone, which is more consistent with the pile-side hole zone shown in Figure 12, indicating that the pile-side rock was broken and filled with pores when the steel pipe pile was penetrated, causing the pile-side frictional resistance to decrease, resulting in a lower pile foundation bearing capacity in the coral reef limestone stratum.

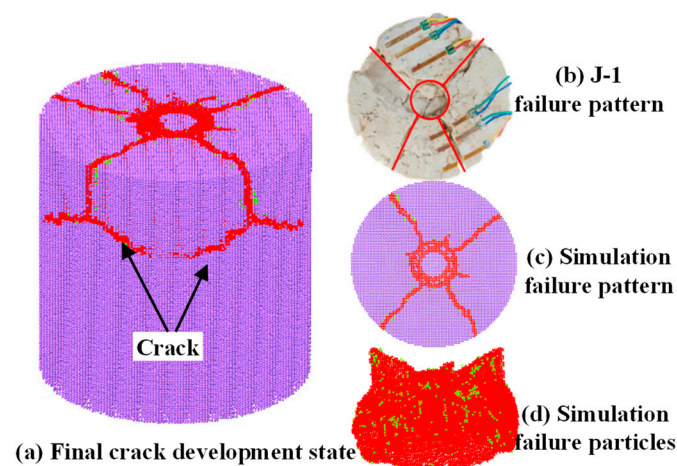


Figure 18. Numerical calculation results of coral reef limestone.

5. Conclusions

For the coral reef limestone at the China–Maldives Friendship Bridge site, after conducting basic physical and mechanical tests on coral reef limestone and steel pipe penetration into the coral reef limestone, the following main conclusions were reached:

1. The strength and elastic modulus of coral reef limestones are low and widely distributed, with strong dispersion. The post-peak stress drop rate of the coral reef limestone is low, and there is local progressive damage, with high residual strength when large deformation is permitted, and the axial strain corresponding to the peak strength is about 1.8%. The red sandstone exhibits typical brittle damage characteristics, the strength decreases rapidly after the peak strength without residual strength, and the axial strain corresponding to the peak strength is about 8%.
2. The high porosity of the coral reef limestone causes the pile top load to possess an obvious sawtooth shape when the steel pipe pile is penetrated. As the penetration depth increases, the pile end load of the high-porosity rock sample gradually decreases, while the pile end load of the low-porosity rock sample slowly increases. In contrast, the pile end load of the red sandstone shows a steady increase with the increase in penetration depth until it is destroyed; the difference between the two may be due to the unique pore structure of coral reef limestone.
3. When the steel pipe pile is penetrated, the farther away from the center of the steel pipe pile, the smaller the strain value of the rock sample. The strain value of the coral reef limestone is about one-half of that of the red sandstone at the same distance from the steel pipe pile, and the extrusion impact of the coral reef limestone stratum during piling is much lower than that of the red sandstone.
4. After the model pile penetrated into the coral reef limestone, the rock on the pile side was shattered, and debris filled the model pile and the coral reef limestone hole wall, and the contact between the pile wall and the coral reef limestone wall was a point-to-point rigid contact with low lateral friction resistance.
5. The simulation of the penetration process by 4D-LSM based on the multi-body damage criterion revealed that the damage particles were mainly concentrated near the annular loading circle, and the main cracks developed in all directions along the end of the specimen with the loading circle at the center and gradually connected, indicating that the rock fragmentation on the pile side during the penetration of the steel pipe pile was the cause of low resistance on the pile side.

The subject of this paper is shallow coral reef limestone driven pile, and the influence of surrounding pressure is not considered. When the bearing mechanism of deep coral reef limestone driven pile is further researched, the influence law of surrounding pressure on

the pile sinking of the driven pile can be studied. The rock strain measurement accuracy can be improved by using higher precision optical fiber sensing technology.

Author Contributions: Methodology, Y.Z.; validation, P.C., H.L. and R.Z.; data curation, C.Y. and C.Z.; writing, Z.D. All authors have read and agreed to the published version of the manuscript.

Funding: This research was supported by the Senior Foreign Expert Project of Hubei Provincial Department of Science and Technology (2021EJD012) and the Technology R&D Project of China Communications Construction Co., Ltd. (2018ZJKJPTJS02).

Institutional Review Board Statement: Not applicable.

Informed Consent Statement: Not applicable.

Data Availability Statement: The study did not report any data.

Conflicts of Interest: The authors declare no conflict of interest.

References

1. Da, B.; Yu, H.; Ma, H.; Tan, Y.; Mi, R.; Dou, X. Experimental investigation of whole stress-strain curves of coral concrete. *Constr. Build. Mater.* **2016**, *122*, 81–89. [[CrossRef](#)]
2. Deshmukh, A.M.; Gulhati, S.K.; Venkatapparao, G.; Agarwal, S.L. Influence of geological aspects on behaviour of coral rock. *Int. Conf. Soil Mech. Found. Eng.* **1985**, *11*, 2397–2400.
3. Agarwal, S.L.; Malhotra, A.K.; Banerjee, R.L. Engineering properties of calcareous soils affecting the design of deep penetration piles for offshore structures. In Proceedings of the 9th International Offshore Technology Conference, Houston, TX, USA, 2–5 May 1977; Volume 3, pp. 503–512.
4. Sun, L.; Wang, Y.; Guo, W.; Yan, S.; Chu, J.; Liu, X. Case study on pile running during the driving process of large-diameter pipe piles. *Mar. Georesources Geotechnol.* **2017**, *36*, 709–721. [[CrossRef](#)]
5. Dutt, R.; Cheng, A. Frictional Response of Piles in Calcareous Deposits. In Proceedings of the Offshore Technology Conference, Houston, TX, USA, 7 May 1984. [[CrossRef](#)]
6. Poulos, H.G.; Randolph, M.F.; Semple, R.M. Evaluation of pile friction from conductors tests. In Proceedings of the International Conference on Calcareous Sediments, Perth, Australia, 15–18 March 1988; pp. 599–605.
7. Wang, X.; Wang, X.Z.; Zhu, C.Q.; Meng, Q.S. Shear tests of interfaces between calcareous sand and steel. *Mar. Georesources Geotechnol.* **2019**, *37*, 1095–1104. [[CrossRef](#)]
8. Zhu, C.; Liu, H.; Wang, X.; Meng, Q.; Wang, R. Engineering geotechnical investigation for coral reef site of the cross-sea bridge between Malé and Airport Island. *Ocean Eng.* **2017**, *146*, 298–310. [[CrossRef](#)]
9. Zhu, C.Q.; Liu, H.F.; Zhang, B. Micro-structures and the basic engineering properties of beach calcarenites in South China Sea. *Ocean Eng.* **2016**, *114*, 224–235.
10. Liu, H.; Zhu, C.; Zheng, K.; Ma, C.; Yi, M. Crack Initiation and Damage Evolution of Micritized Framework Reef Limestone in the South China Sea. *Rock Mech. Rock Eng.* **2021**, *54*, 5591–5601. [[CrossRef](#)]
11. Wang, X.; Shan, H.; Wang, X.; Zhu, C. Strength characteristics of reef limestone for different cementation types. *Geotech. Geol. Eng.* **2020**, *38*, 79–89. [[CrossRef](#)]
12. Palchik, V. Mechanical Behavior of Carbonate Rocks at Crack Damage Stress Equal to Uniaxial Compressive Strength. *Rock Mech. Rock Eng.* **2009**, *43*, 497–503. [[CrossRef](#)]
13. Pappalardo, G. Correlation between P-wave velocity and physical–mechanical properties of intensely jointed dolostones, Peloritani mounts, NE Sicily. *Rock Mech. Rock Eng.* **2015**, *48*, 1711–1721. [[CrossRef](#)]
14. Palchik, V.; Hatzor, Y.H. The Influence of Porosity on Tensile and Compressive Strength of Porous Chalks. *Rock Mech. Rock Eng.* **2004**, *37*, 331–341. [[CrossRef](#)]
15. Elhakim, A.F. The use of point load test for Dubai weak calcareous sandstones. *J. Rock Mech. Geotech. Eng.* **2015**, *7*, 452–457. [[CrossRef](#)]
16. Wan, Z.; Dai, G.; Gong, W. Full-scale load testing of two large-diameter drilled shafts in coral-reef limestone formations. *Bull. Eng. Geol. Environ.* **2018**, *77*, 1127–1143. [[CrossRef](#)]
17. Li, D.-J.; Shi, C.; Ruan, H.-N.; Li, B.-Y.; Li, W.-Y.; Yao, X.-C. Study on shear behavior of coral reef limestone–concrete interface. *Mar. Georesources Geotechnol.* **2021**, *40*, 438–447. [[CrossRef](#)]
18. Liu, H.; Zhu, C.; Wang, R.; Cui, X.; Wang, T. Characterization of the interface between concrete pile and coral reef calcarenite using constant normal stiffness direct shear test. *Bull. Eng. Geol. Environ.* **2020**, *80*, 1757–1765. [[CrossRef](#)]
19. Ghazali, F.; Baghdadi, Z.; Mansur, O. A Comparative Study of Pile Foundations in Coral Formations & Calcareous Sediments. *J. King Abdulaziz Univ. Eng. Sci.* **1990**, *2*, 3–17. [[CrossRef](#)]
20. Liu, H.-f.; Zhu, C.-q.; Meng, Q.-s.; Wang, X.; Li, X.-g.; Wu, W.-j. Model test on rock-socketed pile in reef limestone. *Rock Soil Mech.* **2018**, *39*, 1581–1588. [[CrossRef](#)]

21. Ministry of Water Resources of the People's Republic of China (MWR-PRC). *Chinese Specification of Soil Test (SL 237-1999)*; China Water & Power Press: Beijing, China, 1999.
22. Ministry of Water Resources of the People's Republic of China (MWR-PRC). *Code for Rock Tests of Hydroelectric and Water Conservancy Engineering (SL/T 264-2020)*; Electric Power Press: Beijing, China, 2020.
23. Vászárhelyi, B. Technical note statistical analysis of the influence of water content on the strength of the Miocene limestone. *Rock Mech. Rock Eng* **2005**, *38*, 69–76. [[CrossRef](#)]
24. Liu, H.; Ma, C.; Zhu, C. X-ray Micro CT Based Characterization of Pore-Throat Network for Marine Carbonates from South China Sea. *Appl. Sci.* **2022**, *12*, 2611. [[CrossRef](#)]
25. Ovensen, N.K. The Use of Physical Models in Design: The Scaling Law Relationships. In Proceedings of the 7th European Conference on Soil Mechanics and Foundation Engineering, Brighton, UK, 10–13 September 1979; Volume 4, pp. 318–323.
26. Zhao, G.-F. Developing a four-dimensional lattice spring model for mechanical responses of solids. *Comput. Methods Appl. Mech. Eng.* **2017**, *315*, 881–895. [[CrossRef](#)]
27. Pratomo, F.Y.; Wei, X.; Zou, C.; Zhao, G.-F. Investigation of the shear failure of rock joints using the four-dimensional lattice spring model. *Int. J. Rock Mech. Min. Sci.* **2022**, *152*, 105070. [[CrossRef](#)]
28. Yin, P.; Zhao, G.-F. Numerical study of two-phase fluid distributions in fractured porous media. *Int. J. Numer. Anal. Methods Géoméch.* **2015**, *39*, 1188–1211. [[CrossRef](#)]
29. Zhao, G.-F.; Deng, Z.-Q.; Zhang, B. Multibody failure criterion for the four-dimensional lattice spring model. *Int. J. Rock Mech. Min. Sci.* **2019**, *123*, 104126. [[CrossRef](#)]
30. Li, Q.; Zhao, G.-F.; Lian, J. A Fundamental Investigation of the Tensile Failure of Rock Using the Three-Dimensional Lattice Spring Model. *Rock Mech. Rock Eng.* **2019**, *52*, 2319–2334. [[CrossRef](#)]
31. Li, Q.; Zhao, G.F.; Lian, J. Further development of the distinct lattice spring model for quality blog crack propagation in concrete and its application in underground engineering. *Tunn. Undergr. Space Technol.* **2019**, *92*, 103061. [[CrossRef](#)]
32. Xie, C.; Nguyen, H.; Bui, X.N.; Nguyen, V.T.; Zhou, J. Predicting roof displacement of roadways in underground coal mines using adaptive neuro-fuzzy inference system optimized by various physics-based optimization algorithms. *J. Rock Mech. Geotech. Eng.* **2021**, *13*, 1452–1465. [[CrossRef](#)]